

New 4.75-in. Ultrasonic LWD Technology Provides High-Resolution Caliper and Imaging in Oil-Based and Water-Based Muds¹

Peng Li², Jonathan Lee², Richard Coates², Jing Jin², and Siong Ming Wong²

ABSTRACT

Imaging technologies from azimuthal logging-while-drilling (LWD) tools provide valuable insight into borehole conditions and address multiple drilling and formation evaluation applications, such as wellbore stability assessment and fracture and bedding plane analysis. Although high-resolution images are widely available for water-based mud (WBM) applications, such as from azimuthally focused resistivity tools, their availability in oil-based mud (OBM) applications is limited.

This paper presents a 4.75-in. LWD ultrasonic imaging tool that provides high-resolution borehole caliper and reflection amplitude images, independent of the mud type

used. Analysis of datasets collected by the tool, in OBM with varying mud weights and under multiple drilling conditions, demonstrate the suitability of the imaging technology in boreholes ranging from 5.75- to 6.75-in. diameter. We present log data and analysis from the field tests that illustrate the quality of both the caliper and the reflection amplitude measurement provided by the tool.

The comparison of these datasets with wireline measurements demonstrates the potential for these LWD ultrasonic logs to be the primary imaging solution in applications where the deployment of wireline technologies is either too risky or costly to be considered.

INTRODUCTION

The deliverables from ultrasonic LWD tools can be used to address a wide range of drilling and formation evaluation challenges in both WBM and OBM. For example, caliper measurements are used for calculation of average borehole size to help calculate cement volumes, as a borehole quality indicator for packer placement, and for environmental corrections for other LWD sensors. Borehole ellipse and azimuthal sector images are used for geomechanics analysis, and high-resolution borehole images for the identification of faults and fractures. Reflection amplitude uses include formation porosity estimation and detailed analysis of faults and fractures, and geological and lithological analyses of bedding planes, laminations, and determination of stratigraphic dips.

Borehole imaging technologies based on electrical measurements have been available for conductive WBM on wireline since the late 1980s (Ekstrom et al., 1987) and early 1990s (Davies et al., 1994). Analogous tools were introduced for LWD a decade later (Li et al., 2005; Bittar et al., 2009).

Options for imaging in nonconductive OBM were more

limited, although tools to produce ultrasonic measurements have been available on wireline from the late 1990s (Hayman, et al., 1998), and LWD azimuthal density image tools were introduced in the early 2000s (Ballay et al., 2001). The resolution of density images is largely limited to the spacing between the source and the detectors, and, to some extent, the spacing between the detectors. This is typically several inches, and therefore, the images are not considered high resolution. Although LWD ultrasonic caliper tools, used primarily for compensating other measurements, were introduced in the early 2000s (Labat, et al., 2002), until recently, ultrasonic LWD tools capable of generating high-resolution borehole caliper and reflection amplitude images have not been available.

In this paper, we describe an LWD ultrasonic imaging tool capable of generating these images in both conductive WBM, and nonconductive OBM. The tool layout and principles of operation are described, followed by an overview of the laboratory testing conducted during tool development, and finally results from a number of field trials are presented and discussed.

Manuscript received by the Editor July 23, 2019; revised manuscript received October 22, 2019; manuscript accepted October 23, 2019.

¹Originally presented at the SPWLA 60th Annual Logging Symposium, The Woodlands, Texas, USA, June 17–19, 2019, Paper T.

²Halliburton, 3000 N. Sam Houston Pkwy E., Houston, TX 77032-3219; Peng.li@halliburton.com; Jonathan.Lee@halliburton.com; Richard.coates@halliburton.com; Wong.SiongMing@halliburton.com; Halliburton, 315 Jalan Ahmad Ibrahim, Singapore, 639940; Jing.Jin@halliburton.com

TOOL LAYOUT AND OPERATION

The sensor section of the tool is shown in Fig. 1. It is composed of four transducers positioned at 90° increments around the tool body at the same axial location. Every transducer acts both as a transmitter and as a receiver. Each transducer only detects and records the echo of the pulse it generates, and not the echo of pulses emitted by other transducers. This mode of use is sometimes denoted “pulse-echo”. During the firing stage, all four transducers (acting as transmitters) are excited simultaneously. After a short mute time, all four transducers are activated in parallel (acting as receivers) to acquire four individual inputs. Four azimuthally distributed transducers are used to compensate for tool motion and eccentricity. The tool is equipped with a high-speed digital signal processor (DSP) that analyzes the four channel raw waveforms, performs ringing removal and then echo detection. The tool can perform 500 firings per transducer every second, from which it can acquire and process 2,000 echoes per second. These elements are described in more detail below.

Each transducer is composed of a single circular diced wafer of piezoelectric material, which is diced from the top surface to about 80% of the thickness (see Fig. 1b). The top surfaces of all columns are connected electrically via conductive epoxy, while the bottom surface acts as the other electrode for the driving voltage to be applied to. This special dicing feature has the benefit of providing high power, together with the wide bandwidth of the piezoelectric composite. The design also retains the robustness of a piezo wafer with a complete bottom surface, and facilitates epoxy bonding of the bottom surface onto the backing material, which serves to attenuate the ultrasounds emitting backwards.

The single-wafer transducer design was chosen in preference to other possible designs because it provides stronger driving forces and greater sensitivities. Other

designs, including a ring transducer with multiple concentric piezo rings allowing a dynamic focusing capability (Morys et al., 2011) were considered, but the diced wafer proved preferable due to its higher power with wider bandwidth, which converts to smaller ring-down noise. A strong signal with low ring-down is especially important for the tool to handle logging in heavy mud.

The ultrasonic source pulse is generated by applying voltage on the piezo transducer, and the ultrasonic pulse travels through the borehole fluids, with part of the wave reflected from the borehole wall. By analyzing the traveltime of the pulse wave from transmitting to the echo being received, the transducer standoff, and therefore borehole radius, can be derived given the fluid sound speed. Analysis of the amplitude of the echo signal enables the reflection amplitude of the borehole surface to be derived. The continuous firing of the pulse signal and receiving of the echo while rotating enables radius and reflection amplitude images to be obtained as functions of azimuth and measured depth.

The pulse-echo transmit-receive operation begins with the transducer acting as a transmitter, where electrical energy is applied to the transducer, and through the piezoelectric effect of the wafer, the electrical energy is converted into acoustic energy. Then, operating as a receiver, the wafer senses the reflected ultrasonic echo and converts the associated pressure wave back into electrical voltages that are ultimately digitized. This is our signal of interest, and the one referred to when we discuss signal/noise ratio (SNR) below. The digitized voltages also consist of those generated by ambient acoustic noise, electrical noise from the tool and others in the bottomhole assembly (BHA), and of residual ringing of the transducer caused by the firing pulse. Ambient acoustic noise in the borehole environment decays rapidly with frequency (Joyce et al., 2001), and electronic noise can be minimized by best-practice circuit design. However, the residual ringing of the transducer must be mitigated with special care.

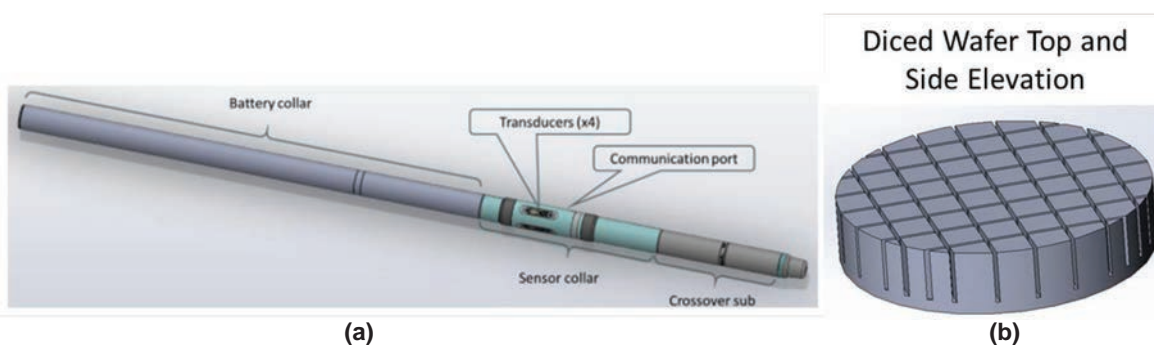


Fig. 1—(a) 4.75-in. ultrasonic imaging tool layout, featuring a sensor section composed of four ultrasonic transducers and a communication port. Stabilizers are recommended on either the battery collar, or the crossover sub or both. (b) A schematic of the diced piezoelectric wafer.

Simply increasing the drive voltage will generate a stronger emitted signal but will also induce higher amplitude ringing. Thus, the resulting SNR may not improve. However, the unique wafer construction of the transducer is designed to achieve both strong transmitting power, high sensitivity, and ensure rapid ringing reduction after firing. Adding a backing material behind the transducer further attenuates residual ringing significantly. Even these steps may not completely solve the problem, particularly in OBM. These muds can attenuate the ultrasonic energy by more than 20 dB/in., i.e., an order of magnitude/inch reduction in signal level in heavy-muds (> 14 lbm/gal). In these circumstances small amplitude echoes can still be buried under transducer ringing noise making them difficult to detect and interpret.

We define the ultrasonic transducer SNR as the peak amplitude of the echo divided by the amplitude of the transducer ringing at the echo detection time. The echo amplitude and detection time are calculated from the recorded waveforms automatically using a proprietary method. Each raw waveform measurement is decomposed in both the time and frequency domains, and then the echo is extracted through a matching filter, to obtain the associated traveltime and amplitude. Both the amplitude and time vary with the standoff of the tool from the borehole wall, and the transducer ringing decays as a function of time. Hence, the SNR also varies with echo arrival time, or equivalently with

standoff. A group of echo-signal measurements with varying standoffs is shown in Fig. 2, illustrating the decay of echo amplitude with standoff. The amplitude of the transducer ringing does not vary with standoff, hence its amplitude at a point in the waveform can be estimated from recordings corresponding to very large standoffs and very late echo times.

The resulting SNR for varying standoff is demonstrated in Fig. 3. The SNR can be seen to degrade as the standoff increases, although the transducer still achieves more than 10 dB SNR over a large standoff range. In our experience, with a SNR above 10 dB, the echo can be reliably extracted automatically.

The transmitter beam pattern was evaluated by placing the transducer in a fixed location and recording it firing with a calibrated hydrophone moved in a three-dimensional (3D) grid pattern in front of the transducer. The amplitude of recording was extracted as indicative of the acoustic pressure at each point. The displays in Figs. 4a and 4b show two orthogonal slices through this 3D volume crossing in front of the center of the transducer. The images show a well-collimated beam transmission pattern out to at least 2-in. standoff.

Similarly, Figs. 4c and 4d show the sensitivity of the transducer operating in reception mode. These were generated using a calibrated source fired on a 3D grid in

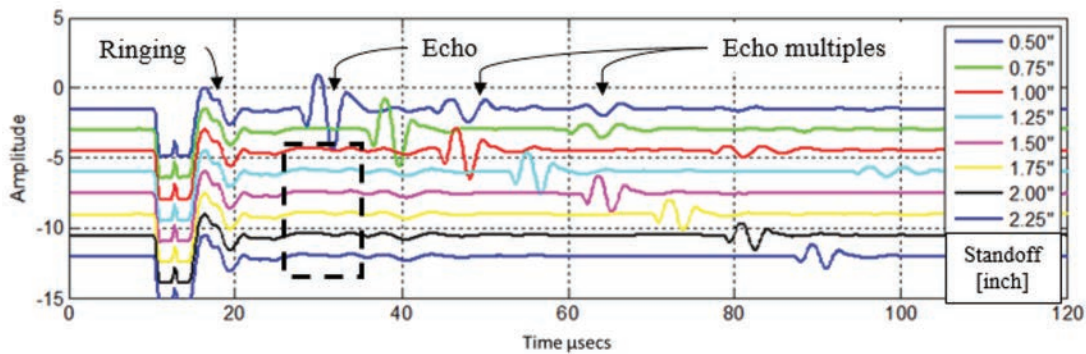


Fig. 2—Transducer echo measurement with different standoff showing a stable echo and consistent ringing. The ringing amplitude for any time can be estimated from waveforms corresponding to large standoffs, e.g., the dashed box contains only ringing for standoffs greater than 0.75-in.

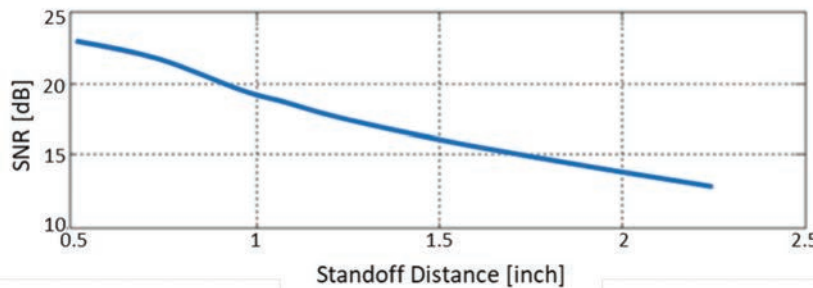


Fig. 3—Transducer SNR response with varying standoff. The SNR remains above 10 dB beyond 2-in. standoff.

front of the transducer. The images show orthogonal slices that cross in front of the center of the transducer. Again, we see a well-collimated response. The collimated nature of the transducer emission and reception patterns are important in producing high-resolution images over a range of standoffs.

The electronics of the tool are composed of three

subsystems that are illustrated in Fig. 5. These are the digitization subsystem, the multiple ultrasonic-transceiver subsystem, and the directional subsystem. The combined electronics system generates the borehole shape and reflection amplitude measurements.

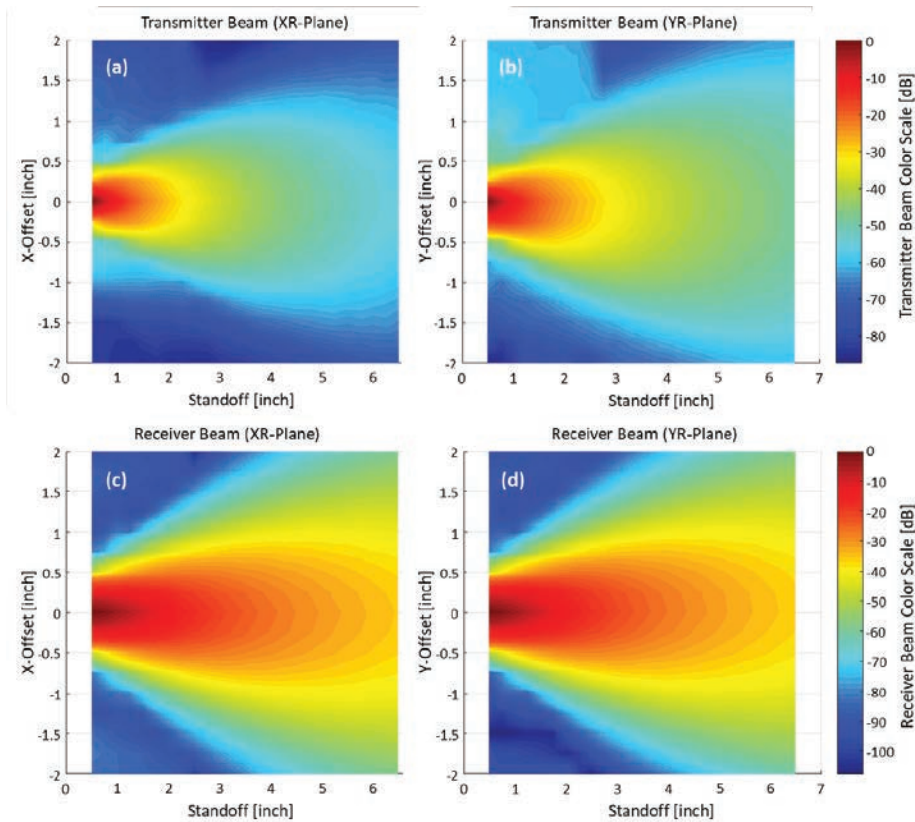


Fig. 4—Transmitter (a) and (b), and receiver (c) and (d) beam pattern in water. The transmitter and receiver beam images are independently normalized to their respective maximum values. The images illustrate that the transducer has a well-collimated response within a 2-in. distance (standoff) for both transmission and reception functions.

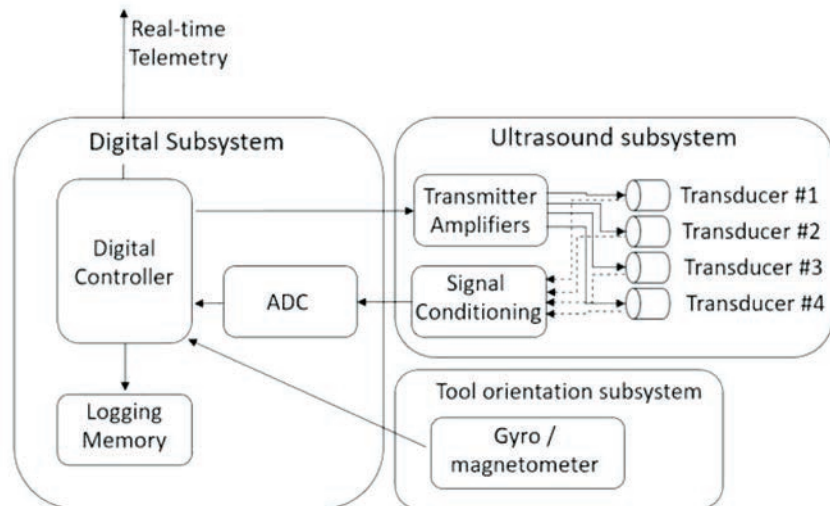


Fig. 5—Block diagram detailing the electronic subsystems.

The ultrasonic-transceiver subsystem is composed of the transmitter amplifier, the analog signal conditioning circuit, and the four ultrasonic transducers. The transmitter amplifier amplifies the firing pulse and applies the high-voltage pulse on the transducer. In order to address the changing attenuation rates of different OBM types and densities, an adjustable power supply is included in the transmitter amplifier so that a different firing voltage can be used for different mud weights. A transmitter/receiver interface circuit is designed to protect the receiver from high-voltage firing signals during the transmitting phase, and also to block the transmitter from loading on receiving paths during the receiving phase. The signal conditioning circuit takes the received charge signals generated from the transducer and amplifies them to a level that is compatible with the analog-to-digital converter (ADC). Appropriate filtering is also included in the signal conditioning circuit to remove nonrelevant switching noises from other parts of the system.

The digital subsystem mainly includes the DSP, the memory components, and the ADCs. The DSP acts as the central control, communication, and processing unit generating the firing reference signals and controlling the transmitter amplifier to enable the firing. In addition, it synchronizes the ADCs to acquire the reflected echoes at the correct echo reflection time. These echoes are processed inside the DSP to generate the transducer standoffs and reflection amplitude values. Gyros and magnetometers are used to acquire the tool-face information during tool rotation. The gyro provides accurate rotational information, and the result is compensated with the magnetometer measurements to remove biasing errors. The tool face is synchronized with the firing pulse to achieve azimuthal standoff and amplitude measurements. The digital processor combines all measurements and processed results together to save into the memory and for transmission to surface.

The accuracy of a conventional wireline mechanical caliper can be affected by both the limited number of arms and borehole spiraling conditions. LWD ultrasonic caliper measurements have the advantage of full-borehole coverage while the sensor is rotating in the drillstring, and therefore, the potential to provide more accurate measurements. However, a number of challenges can affect the accuracy of LWD ultrasonic caliper measurements.

First, the ultrasonic measurement generates a standoff measurement, which represents the distance between the face of the transducer wafer to the borehole wall, and therefore, is not a direct measurement of borehole diameter. The standoff at multiple orientations together with the tool

size are needed to produce a diameter measurement. To minimize the radial motion (eccentering) of the tool we use an undergauge stabilizer, which is a short metal sleeve that is secured over the BHA having an outside diameter (OD) equal to, or a little smaller than the bit size. Consequently, the undergauge stabilizer is slightly smaller than the borehole (hence its name) and serves to minimize, but not eliminate the amount of eccentering the tool experiences.

Second, if the transducer is in too close proximity to the borehole wall, the reflected echo will be hidden beneath the highest amplitude transducer ringing described earlier. To avoid this, and mechanical damage caused by transducers impacting the borehole wall, all four transducers are recessed slightly from the tool's outer diameter. This helps guarantee the minimum standoff required by a pulse-echo measurement and alleviate transducer wear and damage problems.

A final step is real-time ringing removal. This is facilitated by the large amount of memory incorporated in the downhole electronics to store the raw waveform measurement. The transducer ringing components of the waveforms are identified and extracted from the raw waveforms in real time using a proprietary algorithm that identifies invariant portions of the waveforms over an ensemble of multiple firings and subtracts them from adjacent waveforms. Note the ringing may vary with the temperature and pressure experienced by the transducer. To minimize this effect, the estimation of transducer ringing is updated periodically during the drilling run.

Figure 6 illustrates the effect of the implemented ringing removal. Figure 6a shows raw waveforms for a full rotation of the tool plotted as a two-dimensional (2D) azimuthal image. The horizontal axis is the azimuthal angle of the acquired waveform, and the vertical axis indicates the traveltime in microseconds. The amplitude of the waveform is illustrated with a variable density grayscale, with brightness and darkness indicating larger and smaller values, respectively. The heavy black and white stripes in the lower part of Fig. 6a indicate the transducer ringing. The wavelets with variable arrival times in the middle of the displays are the echoes. The varying reflection times result from tool motion and the deviation of the borehole cross-section from circularity. Note the ringing and echo possess similar frequency content, and the ringing component extends to 60 μ sec. Figure 6b shows the same 2D azimuthal image with the ringing removed. This figure only shows the effect of ringing removal; the ringing itself is typically estimated from a much larger ensemble of data. After removal of the ringing it is much easier to extract the echo signal.

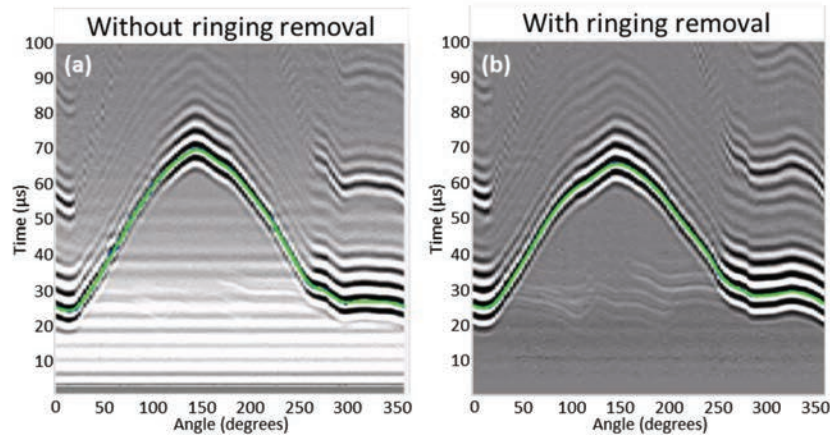


Fig. 6—Transducer ringing removal shown using a variable density display. (a) Raw waveform data from one transducer for one complete rotation of the tool, and (b) the data after transducer ring removal.

In a nonstabilized or poorly-stabilized configuration, tool-body movement during the caliper measurement can be detrimental to the standoff, and corresponding calculated borehole diameter. This is illustrated in Fig. 7a where a 4.75-in. tool is depicted in a 7-in. borehole with enlargement. The center of the tool body is following a circular motion (the motion trajectory shown in red) during the tool rotation. In

this example, the circular motion is off-center with respect to the borehole center, and the tool traverses the trajectory shown in red at the same rate as the tool rotates. As a result, the transducer sees a reduced standoff throughout a full rotation and the generated caliper result (in green) shows the effect of the motion on the caliper measurement (Fig. 7b).

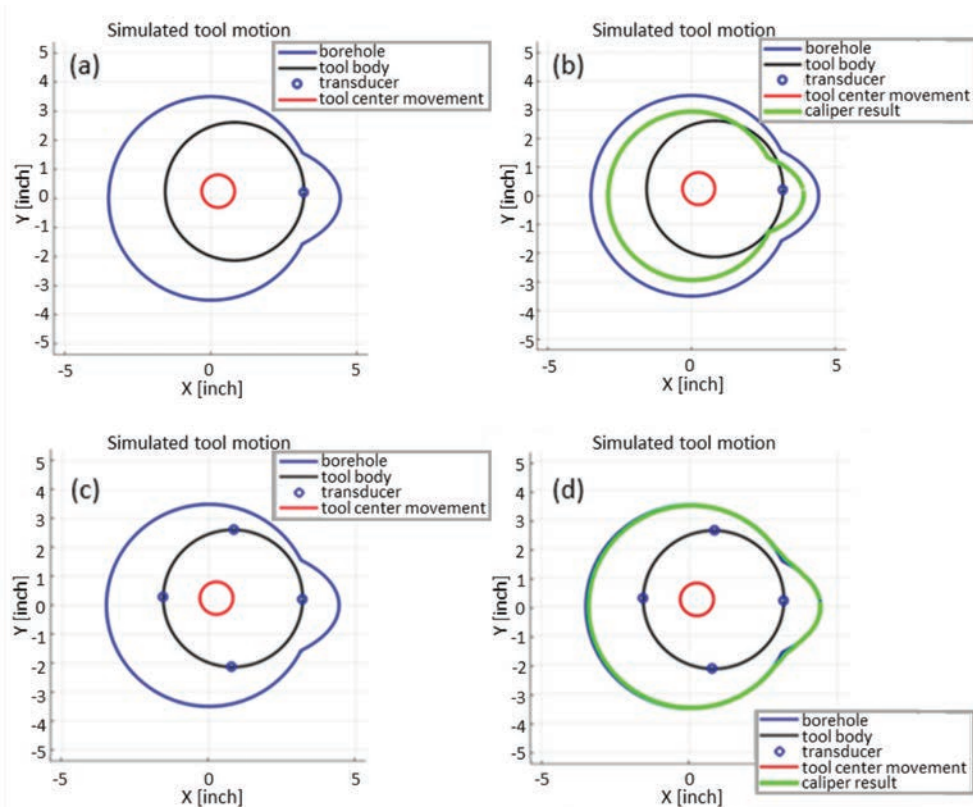


Fig. 7—Schematic representation of the use of multiple azimuthally distributed transducers for tool-motion correction. In this example (a) shows a single transducer (blue dot) mounted on the circumference of a tool (black) whose center traverses a path shown in red as the tool (and transducer) rotates through 360°. (b) Without compensating for tool motion, the inverted borehole shape (green) is systematically smaller than the true borehole (blue). (c) Adding additional transducers distributed azimuthally allows for (d) a more accurate inversion of the borehole shape (green) shown.

The four identical transducers, distributed circumferentially at 90° intervals, allow us to compensate for the tool motion, shown in Figs. 7c and 7d. The motion-correction algorithm relies on the fact that at any given moment standoffs are measured on opposing sides of the borehole and along orthogonal axes. Thus, if the tool is displaced to one side (as in Fig. 7), it is manifest in the raw data as a decreased standoff for one transducer and a corresponding increased standoff for the transducer on the opposite side of the tool. The algorithm uses the fact that the tool measures echo times (borehole standoff) in four orthogonal angles as it rotates. It begins by calculating an approximate borehole shape from these measurements and the associated recorded rotation angles. The tool motion is then calculated by minimizing the difference between measured and modeled echo times by adjusting the assumed tool location for each firing using a least-squared cost function. A refined borehole shape can then be calculated. This removes the requirement for an assumed borehole shape, e.g., circular or elliptical, which is a feature of some borehole-shape algorithms.

The speed of sound in mud is an input into the borehole diameter and shape calculation. The mud speed is known to depend upon mud composition, temperature, and pressure. We use two steps to determine the appropriate speed. First, a casing calibration is performed where the ratio of the known internal casing diameter to the measured echo time is used to calculate the speed of sound in the mud. Second, an environmental correction to that speed is applied, based on temperature and pressure changes to account for varying downhole conditions.

A big challenge in obtaining a continuous high-resolution image is the downhole system's computational power and memory space. High-resolution images require an uninterrupted, rapid firing rate and high-density data throughput on the downhole electrical system. With a limitation on downhole memory size, the downhole computer may not have the capacity to save all the raw waveforms for surface post-processing when long drilling or logging runs are anticipated. To overcome this challenge, the downhole computer processes all the raw waveforms in real time and saves the traveltimes and reflection amplitude results.

LABORATORY DETECTION AND RESOLUTION QUANTIFICATION

The detection and resolution capabilities of the transducers are important system characteristics. Detection refers to the smallest size and magnitude of an isolated feature that can be seen. Resolution refers to the smallest

distance between adjacent features that allows them to be discriminated. To investigate these transducer characteristics the 2D scanning system, shown in Fig. 8, was constructed in the laboratory to evaluate the transducer's ability to generate images from various features.

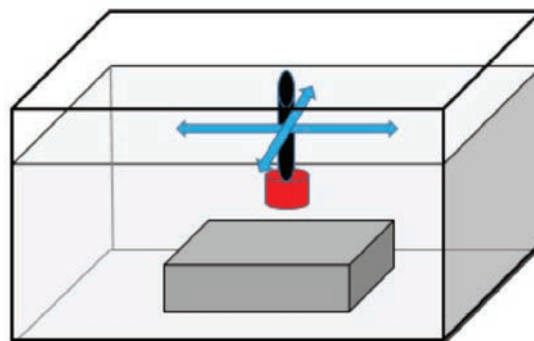


Fig. 8—A schematic representation of the transducer imaging scanning system used for the initial laboratory testing setup. The transducer (red) can scan in a horizontal plane using two orthogonal stepper motors above the target, all immersed in fluid. The height of the transducer above the target may also be adjusted.

A target sample was placed at the bottom of a fluid-filled tank. The transducer was mounted on a slider frame driven by two stepper motors operating in orthogonal directions. This enabled motion in the horizontal plane above the sample. A data acquisition system controls the motor drivers to drive the stepper motors, controls the driving circuit to generate a firing pulse, and interfaces with the preamplifier and signal conditioning circuit to acquire the echo after the firing pulse. A number of tests were conducted on samples designed to evaluate the transducer's ability to identify individual features (detection) and its ability to distinguish the separation between two closely spaced features (resolution).

The first test was designed to study detection. The target was an acrylic block drilled with holes of different diameter and depth. Each hole was sufficiently separated from the others so as not to interfere with each other. The size and pattern of the holes drilled in the acrylic sample are shown in Fig. 9a.

The raw amplitude image created from the transducer moving over the sample at a standoff of 0.5 in. is shown in Fig. 9b, and demonstrates that under the test conditions the transducer detects all the holes, including the two with 0.1-in. diameters and depths of 0.1 and 0.2 in. Note, that while all the holes were detected there is no simple relationship between the amplitude of the ultrasonic image and the diameter and depth of the holes.

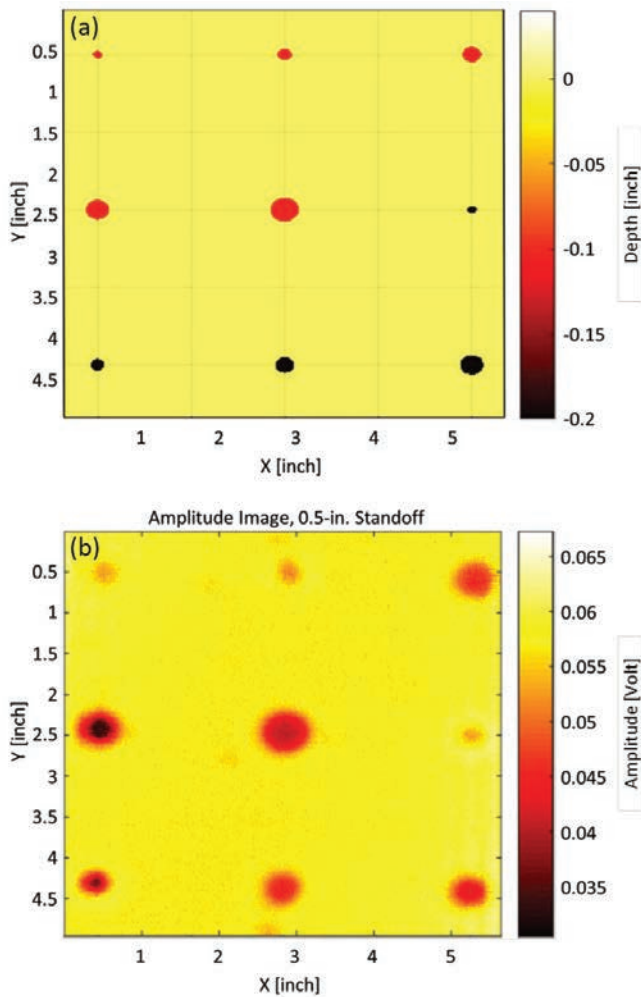


Fig. 9—(a) Schematic of the acrylic test sample, and (b) ultrasonic image used to evaluate feature detection. The targets were holes of varying diameter (0.1, 0.2, 0.25, 0.5 in) and depth (0.1 and 0.2 in).

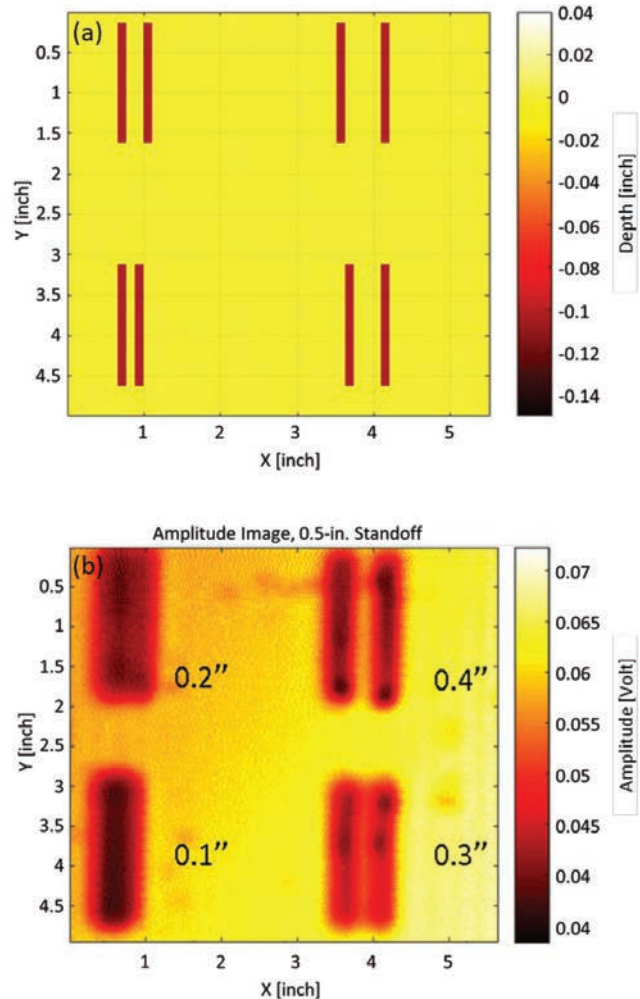


Fig. 10—(a) The schematic of grooves of 0.1-in. depth and 0.1-in width engraved in pairs in the surface of an acrylic block. The grooves were 0.1, 0.2, 0.3 and 0.4 in. apart. Each pair was sufficiently separated from the next that there was no acoustic interference. (b) The ultrasonic image result from scanning the transducer in a 2D plane above the target with a standoff of 0.5 in.

The second test was conducted to assess the ability of the transducer to distinguish two closely situated features as separate objects (resolution). Again, an acrylic block was used with parallel slots engraved in the surface with varying distance between them, as illustrated in Fig. 10a. Four pairs of thin cuts of 0.1-in. width and 0.1-in. depth were engraved closely together, with distances of 0.1, 0.2, 0.3, and 0.4 in. between each pair. Each pair was separated sufficiently to ensure there was no interference between pairs.

The 2D scanning equipment and procedure used were the same as for the first test. The raw image results are shown in Fig. 10b. The image shows that under the test conditions (in water, with a standoff of 0.5 in.), the transducer resolved a separation between the 0.1-in. wide cuts when the separation between members of the pair was ≥ 0.3 in., but not when the

separation was ≤ 0.2 in.

A third test was conducted to simulate the transducer response to fluid-filled fractures. A cement brick broken through its complete thickness was used to mimic a fracture. The two halves of the brick were positioned at varying separations from one another to simulate different fracture widths, as illustrated in Fig. 11. The test was performed in water with a 2-in. standoff. The dashed green boxes in the upper row shows the approximate area covered in the middle and lower images. The gradient in the travelt ime image reflects slight misalignment between the scanner plane and the brick surface.

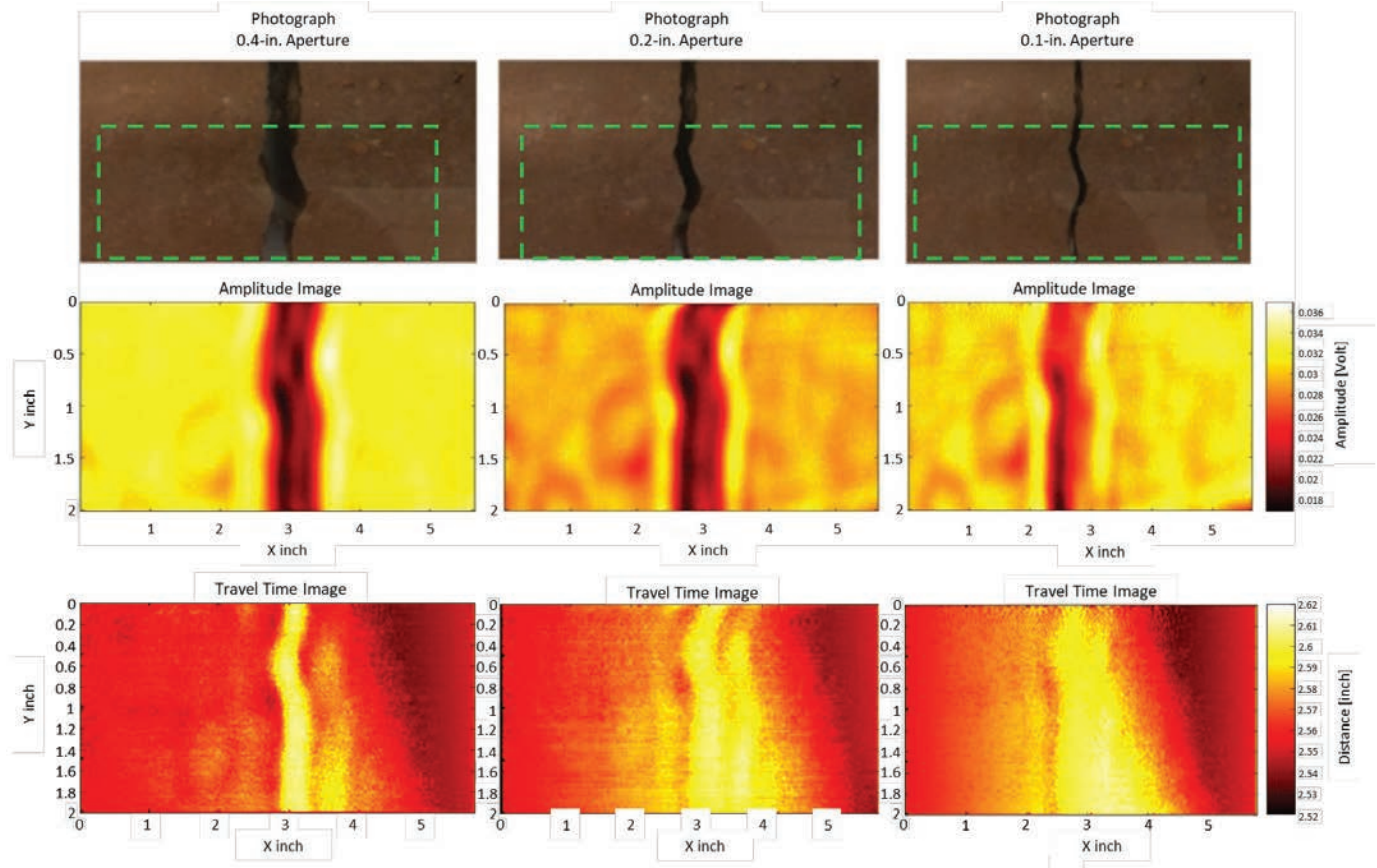


Fig. 11—Cement-block fracture imaging with a 2-in. standoff. The upper row shows photographs of the cement block with varying fracture apertures; the middle row shows the reflection amplitude image; and the lower row shows the standoff image obtained from echo times.

The raw amplitude image clearly detects all the fractures, including the 0.1-in. aperture fracture. Note the standoff image is less sensitive, with the 0.4-in. aperture fracture detectable, the 0.2-in. fracture marginal, and the 0.1-in. fracture almost undetectable. Although the fracture with a 0.1-in. aperture is clearly seen in the 2-in. standoff image, it is more clearly resolved when the experiment was repeated in water with a standoff of 0.5 in. (Fig. 12). The dashed green box in the upper image shows the approximate area covered in the lower images, and again the gradient in the travelttime image reflects slight misalignment between the scanner plane and the brick surface.

Both Figs. 11 and 12 show that the transducer standoff image obtained from the echo traveltimes is less sensitive to small fractures than the amplitude image. This can be explained with reference to Fig. 4, where we see that a signal integrates contributions from a finite area of the target

illuminated by the beam. Thus, the echo time is controlled by the earlier portions of the signal reflected from either side of the fracture but within the beam illumination, while the amplitude is more affected by destructive interference between the reflections from inside and outside the fracture. Therefore, travelttime, and hence, the standoff image, is less sensitive than the amplitude image to small features on the borehole surface. Conversely, the borehole rugosity has a greater impact on the echo amplitudes when the surface roughness is comparable to the ultrasonic wavelength.

Having verified transducer performance under the limited test conditions offered by the 2D setup, a 3D rotating apparatus was constructed to evaluate the transducer's azimuthal measurements. In order to simulate downhole conditions as closely as possible, the 3D system setup included four transducers and the downhole electronics as part of the hardware, as illustrated in Fig. 13.

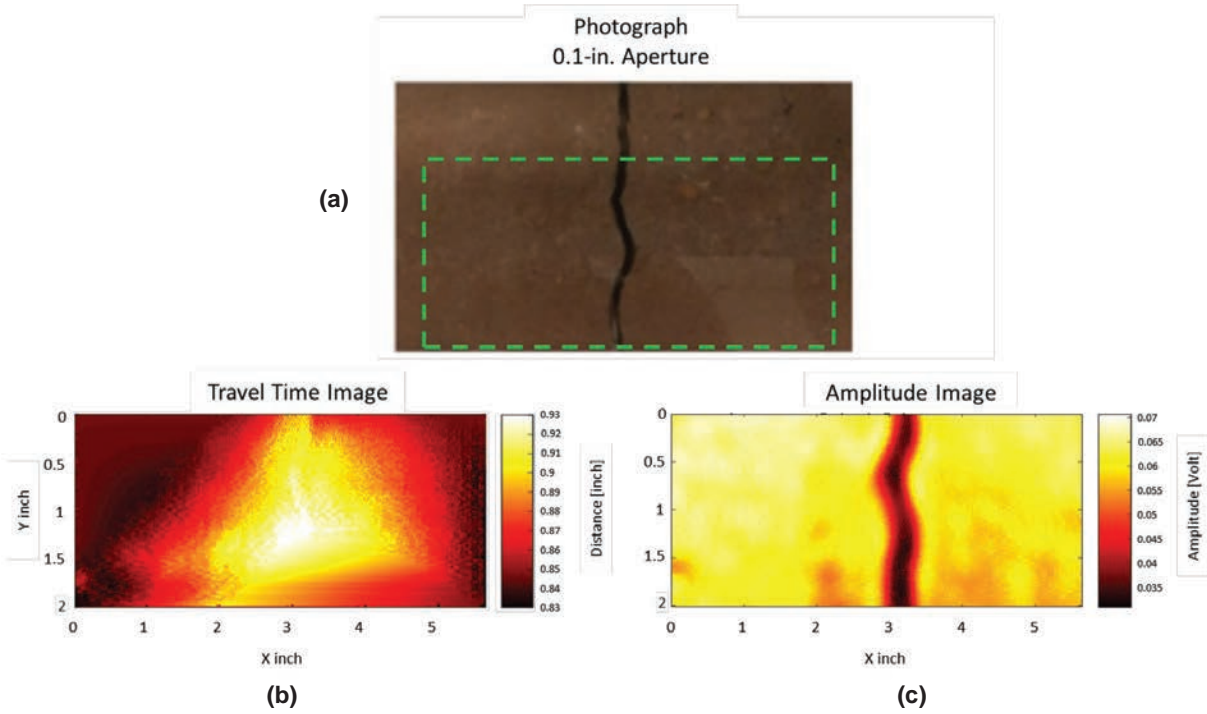


Fig. 12—Cement block fracture imaging with 0.5-in. standoff. (a) A photograph of the cement block with 0.1-in. fracture aperture. The lower row shows the standoff image determined from (b) the echo times, and (c) the reflection amplitude image.

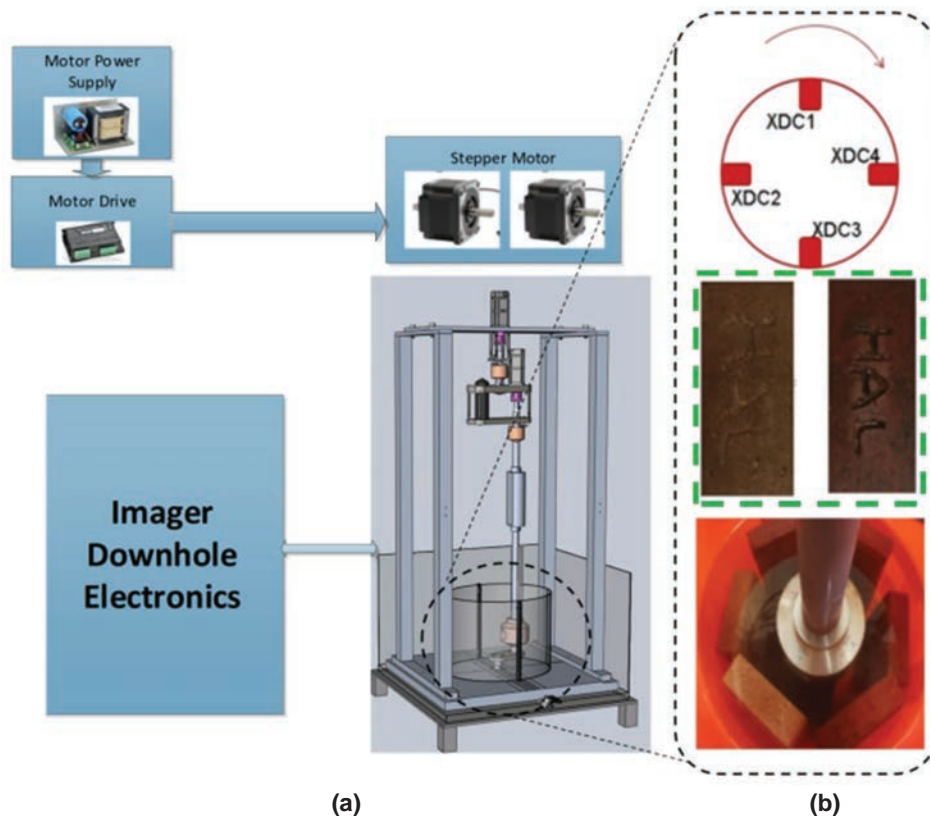


Fig. 13—The 3D rotating laboratory equipment for system-level verification. This setup tested the transducers integrated with the downhole electronics. Figure 13b shows an enlargement of a cross section of the transducer assembly (top); two of the target blocks in the dashed-green box, hand-engraved with the letters “HAL” (middle) and a photograph of the test assembly from above (bottom).

In the 3D setup, two-axial rotational movements are controlled by two stepper motors, and the z-axis motion is controlled by a linear driver. The four transducers were mounted on a head that could be immersed in the drilling fluid containers. In the same way that the combined tool would operate downhole, the setup was directly controlled by the downhole electronics, with synchronized firings and directional measurements being obtained. The test samples used were six concrete bricks, two of which had the letters “HAL” hand-engraved on them.

Figure 14 shows the reflection amplitude images from the rotating test, conducted in water for the individual transducers without compensating for the azimuthal position of the transducers. Thus, each image is rotated by 90° from its adjacent image, reflecting the fact the transducers were located at 90° increments around the assembly. Note that towards the edge of the bricks, specular reflection is not detected by the transmitter.

The laboratory testing described, and further testing discussed by Li et al. (2019), verified the potential for the combined four-transducer configuration to provide caliper measurements and generate traveltimes and reflection

amplitude images in both WBM and OBM. The transducers were incorporated into two 4.75-in. collars, and prepared for field trials.

FIELD TEST COMPARISON WITH WIRELINE TECHNOLOGIES, DIFFERENT LOGGING PARAMETERS AND MUD WEIGHTS

A field test of the tool was conducted at a test rig in Cameron, Texas, USA. For the first trial run, one tool with a 0.25-in. undergauge stabilizer was placed within a BHA comprising a 6.25-in. bit, a 4.75-in. mud motor, a 4.75-in. pressure-while-drilling (PWD) sub, a measurement-while-drilling (MWD) tool, and gamma-ray sensors. The well plan involved logging through a 9.625-in. casing shoe set at 1,290 ft measured depth (MD) and 12.25-in. rathole to 1,380 ft MD and drilling a new borehole while building from vertical with a 10°/100 ft dogleg to an inclination of 45°. This allowed evaluation of images in both vertical and deviated sections. The first section was drilled using 9.5-lbm/gal OBM. The logged section allowed for assessment of sensor performance within a number of different formations,

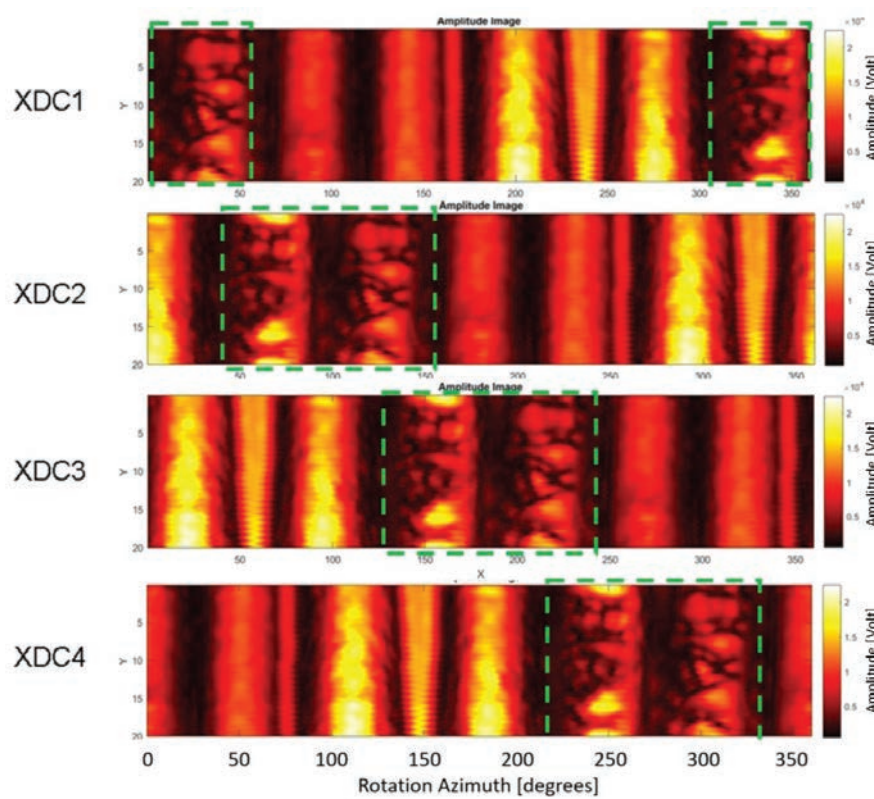


Fig. 14—Reflection amplitude image of the six target bricks for one complete rotation of the 3D rotating apparatus. Each row corresponds to data from a single transducer. Note the dark vertical stripes are the gaps between the bricks where no reflection was detected. The dashed-green boxes highlight the location of the two bricks containing the hand-engraved letters “HAL”.

as shown in Fig. 15. Average drilling rate of penetration (ROP) was 60 ft/hr, with string rotation maintained at 40 rev/min (RPM).

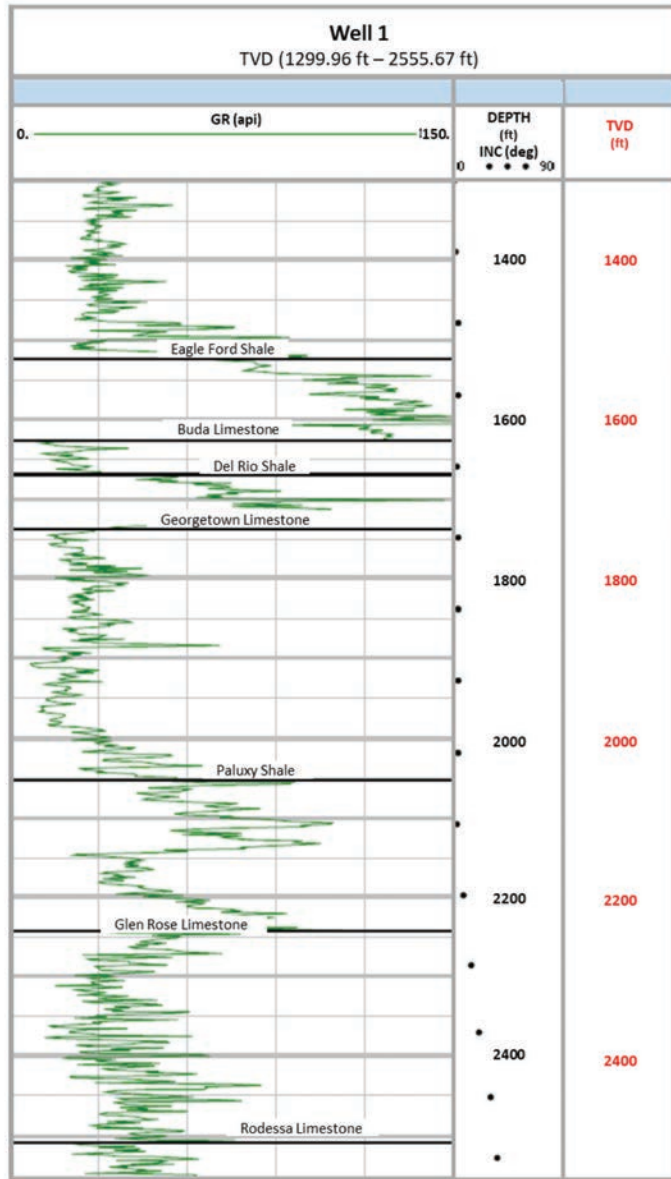


Fig. 15—The well inclination and major formation tops (based upon offset vertical well gamma-ray log correlation) for Well 1. The formation above the Eagle Ford Shale is the Austin Chalk. The vertical and deviated sections of the well are shown.

After landing the well at 45° at 2,669 ft MD, and having acquired 1,289 ft of while-drilling data, the drilling assembly was pulled out of hole, and two wireline runs were

performed to collect high-resolution ultrasonic imaging and pipe-conveyed 6-arm multifinger caliper data. Both datasets were evaluated to identify zones of interest over which a series of wipe runs was performed using the 4.75-in. ultrasonic imaging tool.

Comparison of LWD caliper with the average caliper (obtained from the mean value from each arm) and maximum caliper (obtained from the maximum value of 180° separated pairs of arms) from the multifinger caliper tool showed excellent correlation throughout the drilled section (Fig. 16). The caliper data from both LWD and wireline show that the borehole is slightly overgauge for the majority of the drilling run. Separation between the LWD caliper and the wireline caliper in deviated sections is attributed to the wireline tool not being perfectly centralized within the borehole (Li et al., 2019).

The wireline data also identified a zone of interest between 1,360 and 1,420 ft MD, interpreted as fractures within the Austin Chalk formation. The log example shown in Fig. 17 compares the ultrasonic imaging data from the wireline run with the corresponding reflection amplitude and radius data from the LWD drilling run over a short section of the zone of interest. In general, the images show agreement, with the reflection amplitude images showing more detail than the caliper images, and the LWD images showing a little more detail than the wireline images. The interpreted fractures, highlighted in the green box on the LWD amplitude image, are most prominent on the amplitude images, but are also visible on the radius images. However, there is one significant difference; a vertical feature to the left of center of both the wireline caliper, and more clearly, the wireline amplitude images. This corresponds to a gouge or scratch in the borehole wall of at least 20-ft length, which we believe was caused by the wireline itself or one of the centralizers required for the wireline ultrasonic tool. Obviously, this feature is not present on the LWD data, which were recorded as the borehole was drilled.

Figure 18 shows a further comparison of the wireline and the LWD images in the Eagle Ford Shale and Buda Limestone formations. Again, both sets of images have much in common, this time illustrating borehole characteristic of drilling with a bent mud motor. The amplitude images show more contrast than the caliper images with the LWD caliper images showing more details than the wireline. As in the previous image, a wireline gouge can be seen in the top-right corner of the wireline amplitude image.

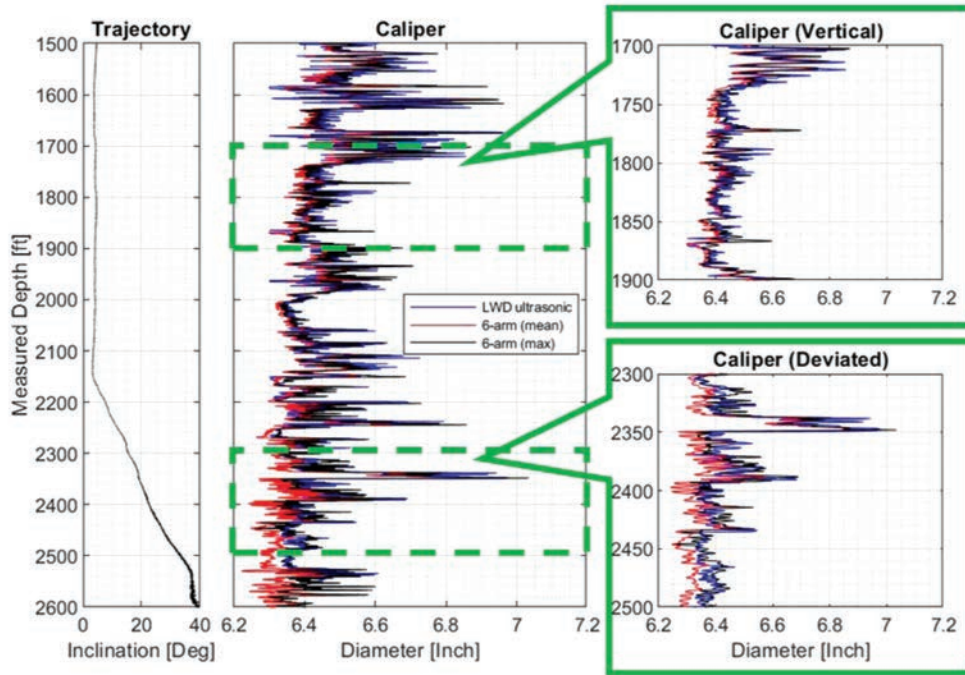


Fig. 16—Comparison of LWD caliper and wireline 6-arm caliper data. The left track shows the well trajectory. The center track shows the LWD ultrasonic caliper data (blue), the 6-arm wireline average caliper (red) and maximum caliper (black). The right track shows details of the caliper in the near-vertical (top) and deviated (bottom) well sections.

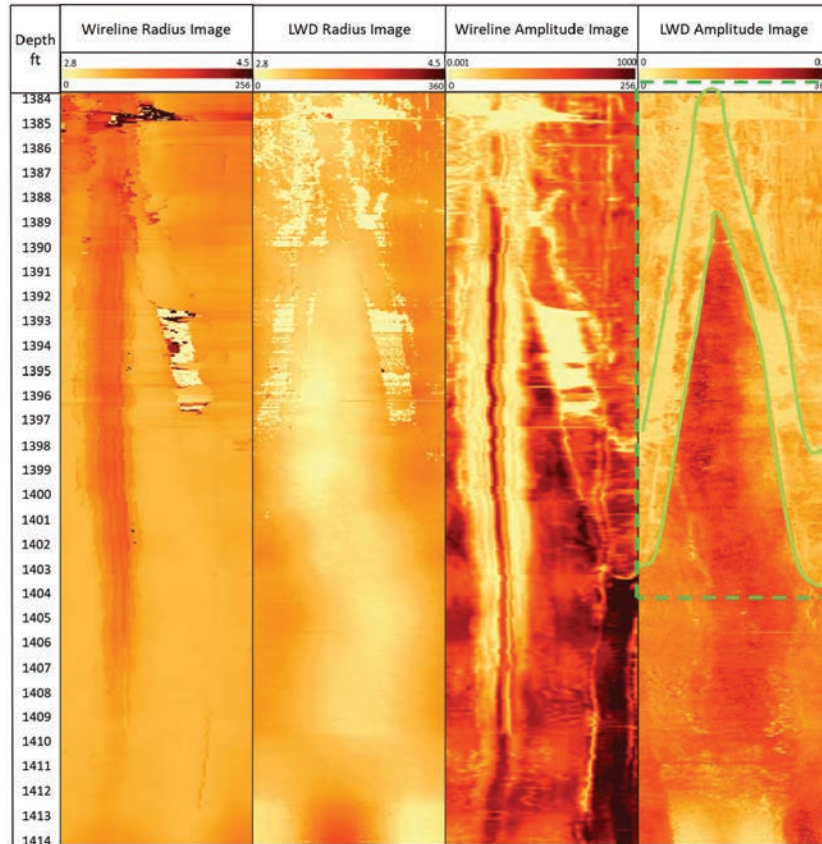


Fig. 17—Log section comparing wireline data with LWD over a short section within the Austin Chalk formation. Track 2, wireline radius image; Track 3, LWD radius image; Track 4, wireline reflection amplitude image; Track 5, LWD reflection amplitude image. The radius images are on the same color scale, but the amplitude images have been independently scaled. Two fractures are shown in green in Track 5.

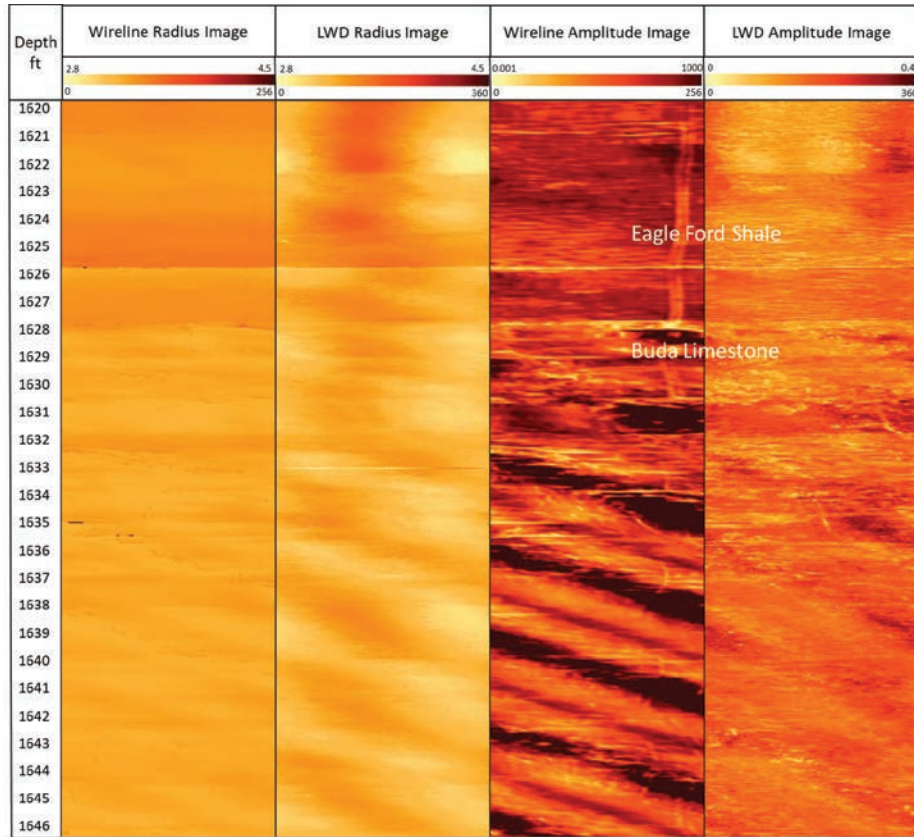


Fig. 18—Log section comparing radius and reflection amplitude images from wireline data with LWD within the Eagle Ford Shale and Buda Limestone formations. Borehole spiraling is observed in each of the images. The radius images are on the same color scale, but the amplitude images have been independently scaled.

The fractures within the Austin Chalk formation were then logged multiple times in wipe mode by the LWD tool within the BHA while tripping in hole (denoted as TI) with varying logging speeds and drillstring RPM with 9.5-lbm/gal OBM. The use of different combinations of ROP and RPM during the wipe runs allows us to evaluate the influence of each on image quality. The relevance of logging speed and drillstring rotation to image quality is illustrated schematically in Fig. 19. Rapid rotation and slow penetration

have the potential to produce finer axial resolution than slower rotation and faster penetration. Thus, the ratio ROP/RPM is the critical parameter.

Table 1 shows the parameters for each logging pass. Note, that from these passes the highest data density (measured in total samples/ft) is obtained with the slowest logging speed (the tool fires at a constant 500 samples/transducer/sec), in this case 30 ft/hr. However, the best axial resolution is expected from a logging speed of 59 ft/hr and 160 RPM due to the resulting low ROP/RPM ratio.

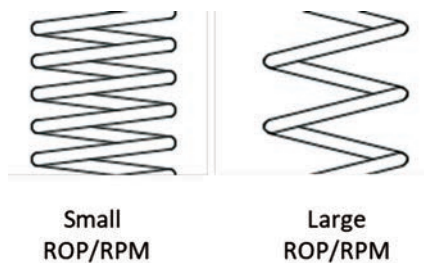


Fig. 19—Schematic illustration of the effect of varying the ratio ROP/RPM on potential axial resolution of images for a single transducer. For slow penetration and rapid rotation, the transducer moves only a small distance axially during each rotation. For rapid penetration or slow rotation, the transducer moves a long distance axially for each rotation.

Table 1—Logging Conditions for Wipe Passes Between 1,370 and 1,450 ft While Tripping in Hole (TI) With 9.5-lbm/gal OBM

Section	ROP (ft/hr)	RPM	Mud Weight (lbm/gal)	ROP/RPM
T11	30	40	9.5	0.15
T12	53	40	9.5	0.27
T13	59	80	9.5	0.15
T14	59	160	9.5	0.07
T15	88	80	9.5	0.22
T16	176	80	9.5	0.44
T17	352	80	9.5	0.88
T18	733	80	9.5	1.83

Figure 20 illustrates the high-resolution reflection amplitude (a) and radius (b) images from the eight wipe passes. Despite the wide range of logging speed and RPM combinations, the notable fracture features observed around 1,390 ft are clearly visible for each wipe pass. The images in

Fig. 20 confirm the predictions shown in Table 1. The near-vertical feature below the fractures, believed to be a gouge mark from the wireline tools, appears progressively less prominent from left to right, suggesting the feature is being eroded by each wipe pass.

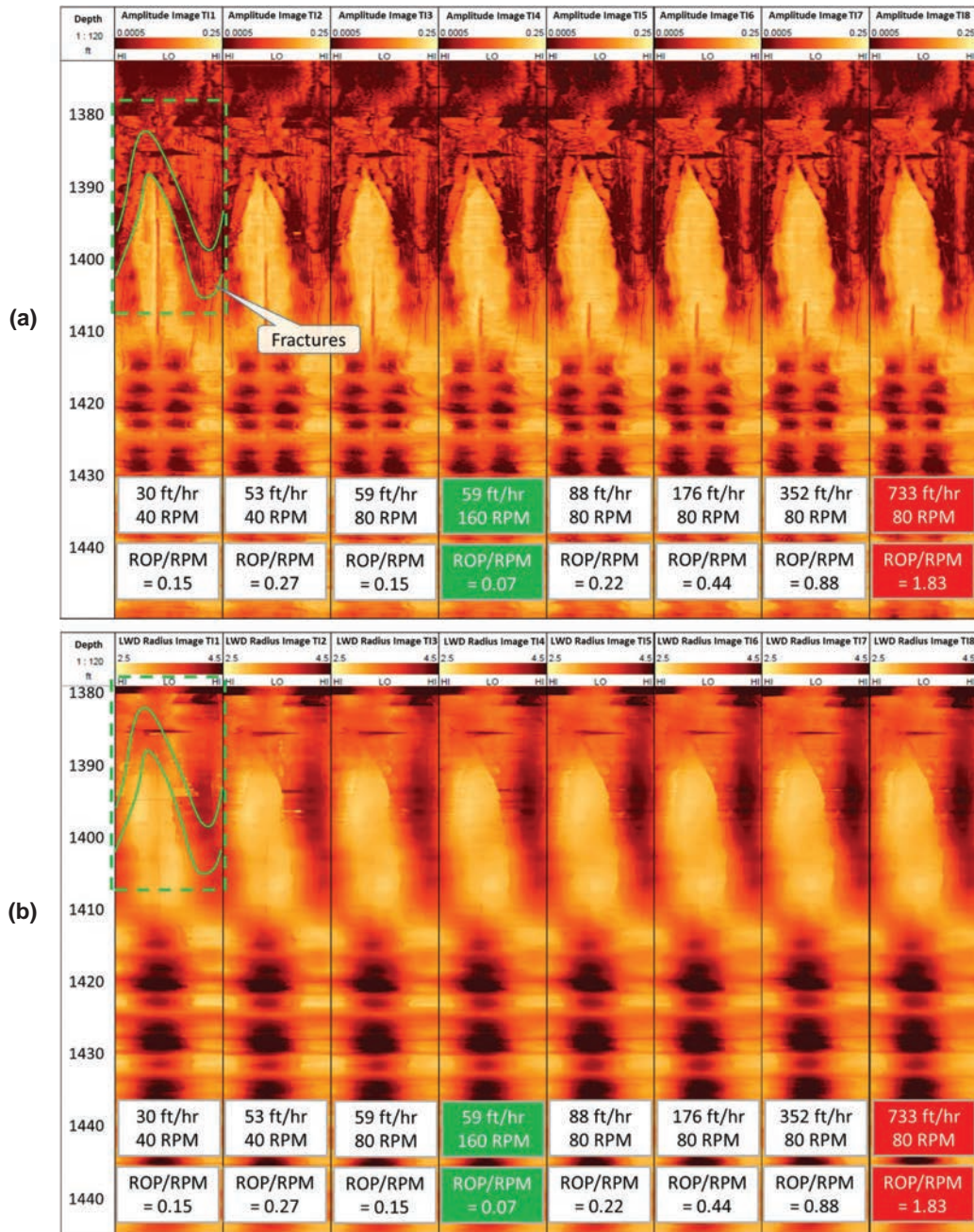


Fig. 20—Reflection amplitude images (a) and radius images (b) from the wipe passes between 1,370 and 1,450 ft while tripping in hole with 9.5-lbm/gal OBM. The logging speed and string rotation, and the ratio of penetration to rotation rate (ROP/RPM) are listed for each example with the lowest and highest, corresponding to the best and worst axial resolution, highlighted in green and red, respectively. The approximate locations of the fractures are shown by the green lines in the top-left panel.

Having completed the wipe passes with 9.5-lbm/gal OBM mud, the well was then displaced to 11.5-lbm/gal OBM and a sequence of wipe runs over the same section of interest was performed while tripping out of hole (denoted as TO) in order to evaluate the impact of different mud weights on the images. The logging conditions for the trip-out wipe passes are shown in **Table 2**.

In Fig. 21, the reflection amplitude (a) and radius (b) image wipe pass plots with 11.5-lbm/gal mud weight again show the highest data density plots occur when the logging speed is slowest (TO1), with a logging speed of 30 ft/hr and string rotation of 40 RPM, and the smallest axial resolution seen during the TO10 pass with a logging speed of 59 ft/hr and 160 RPM string rotation. The fractures within the Austin Chalk are identifiable on all of the reflection amplitude and radius images.

Table 2—Logging Conditions for Wipe Passes Between 1,370 and 1,450 ft While Tripping Out of Hole (TO) With 11.5-lbm/gal OBM

Section	ROP (ft/hr)	RPM	Mud Weight (lbm/gal)	ROP/RPM
TO1	30	40	11.5	0.15
TO2	59	40	11.5	0.30
TO3	59	80	11.5	0.15
TO4	88	80	11.5	0.22
TO5	176	80	11.5	0.44
TO6	352	80	11.5	0.88
TO7	733	80	11.5	1.83
TO8	176	160	11.5	0.22
TO9	88	160	11.5	0.11
TO10	59	160	11.5	0.07

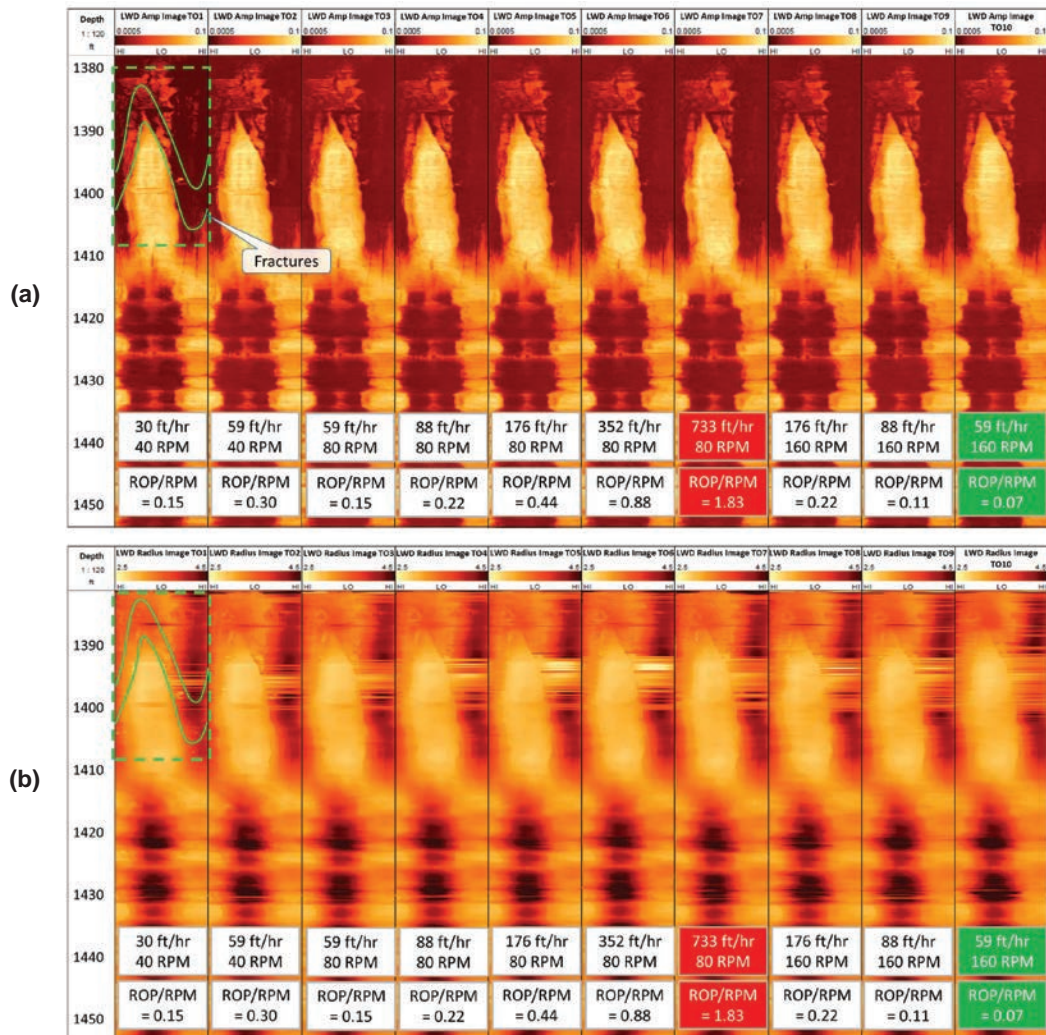


Fig. 21—Reflection amplitude images (a) and radius images (b) from the wipe passes between 1,370 and 1,450 ft while tripping out of hole with 11.5-lbm/gal OBM. The logging speed and string rotation, and the ratio of penetration to rotation rate (ROP/RPM) are listed for each example with the lowest and highest, corresponding to the best and worst axial resolution, highlighted in green and red, respectively. The approximate locations of the fractures are shown by the green lines in the top-left panel.

The drilling data from the 4.75-in. ultrasonic imaging tool showed excellent correlation with both the caliper measurements from the wireline multifinger caliper, and the radius and reflection amplitude images from the wireline high-resolution OBM imaging tool. The impact of logging speed and string rotation variations on LWD image quality was assessed and highlighted how the ROP/RPM ratio determines the axial resolution of the images. Assessment of image quality in different mud weights was made, with high-resolution images obtained in both 9.5- and 11.5-lbm/gal OBM.

FIELD TEST TO DETERMINE IMPORTANCE OF STABILIZATION IN VERTICAL WELL

For the second trial run, a 6.125-in. vertical well was drilled with 9.5-lbm/gal OBM off the same primary wellbore used for Well 1 (open hole drilled from below the same 9.625-in. casing shoe). The main objective of the run was to evaluate the impact of decentralization of the tool in a vertical well on the quality of the images. Two 4.75-in. tools were included in the BHA, one tool with a 0.125-in. undergauge stabilizer, i.e., with OD of 6 in., and the second tool without any stabilization. The vertical well also allowed for assessment of both borehole caliper and image quality through a wide range of formations, as shown in Fig. 22, which highlights the major formations through which the tools were logged.

The 256-sector reflection amplitude images shown in Fig. 23 are from a section of the Austin Chalk formation. In Fig. 23a the image on the left is from the nonstabilized tool, and shows significant “blurring” compared to the image on the right from the stabilized tool. The images from both tools clearly show striations believed to be caused by a section of the mud motor, shown in Fig. 23b. The dark areas on the nonstabilized tool image from 1,428 to 1,444 ft and from 1,452 to 1469 ft, indicate that there was greater standoff, resulting from eccentricity. For reference, each of the circular features on the kickpad is 0.605 in. in diameter.

The vertical well field trial illustrated the importance of stabilizing the 4.75-in. ultrasonic imaging tool in order to minimize the impact of decentralization on the image quality in OBM. High-resolution radius and reflection amplitude images were collected through multiple formations, allowing future assessment of fractures and bedding features in shale, limestone, and sandstone formations.

FIELD TEST TO EVALUATE IMAGES IN HIGH-ANGLE WELL

A third trial well was drilled with 9.5-lbm/gal OBM, building from vertical to horizontal in order to assess both caliper measurements and image quality in a high-angle wellbore. As with Well 2, the wellbore was drilled from below the same 9.625-in. casing shoe as Well 1. The hole was drilled with a mud motor, and a fully stabilized tool was run with 0.125-in. undergauge stabilizers placed directly above and below the tool to minimize decentralization and its potential impact on image quality.

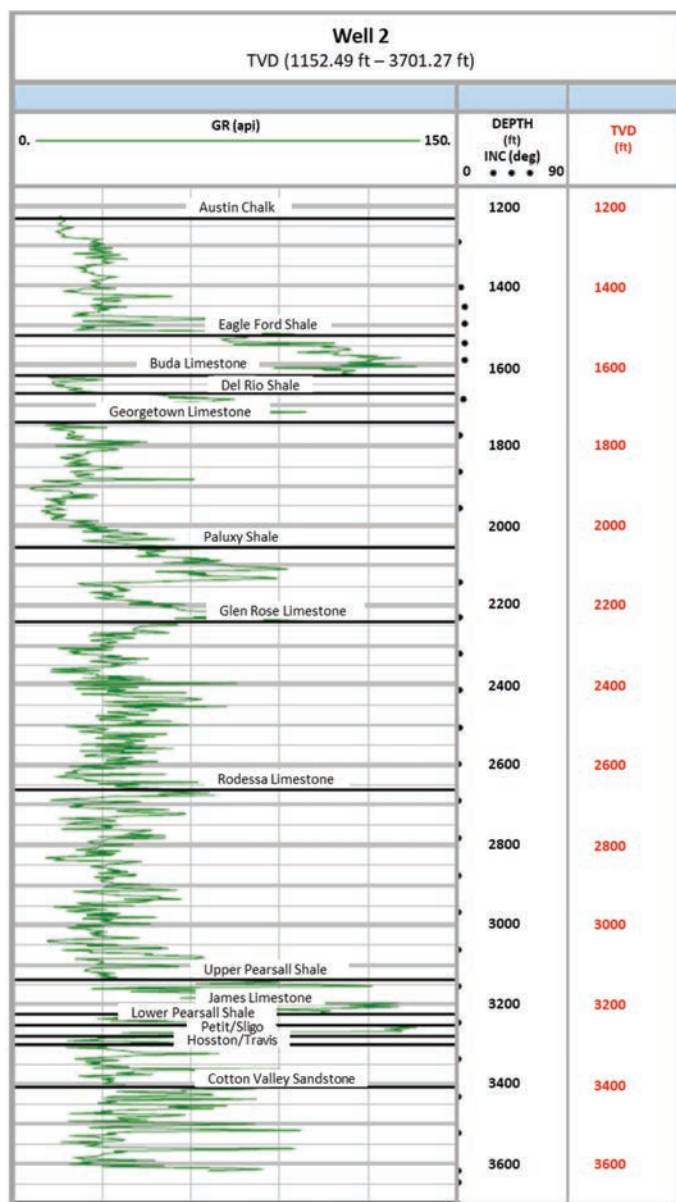


Fig. 22—Well 2 inclination and major formation tops based upon offset vertical well gamma-ray correlation.

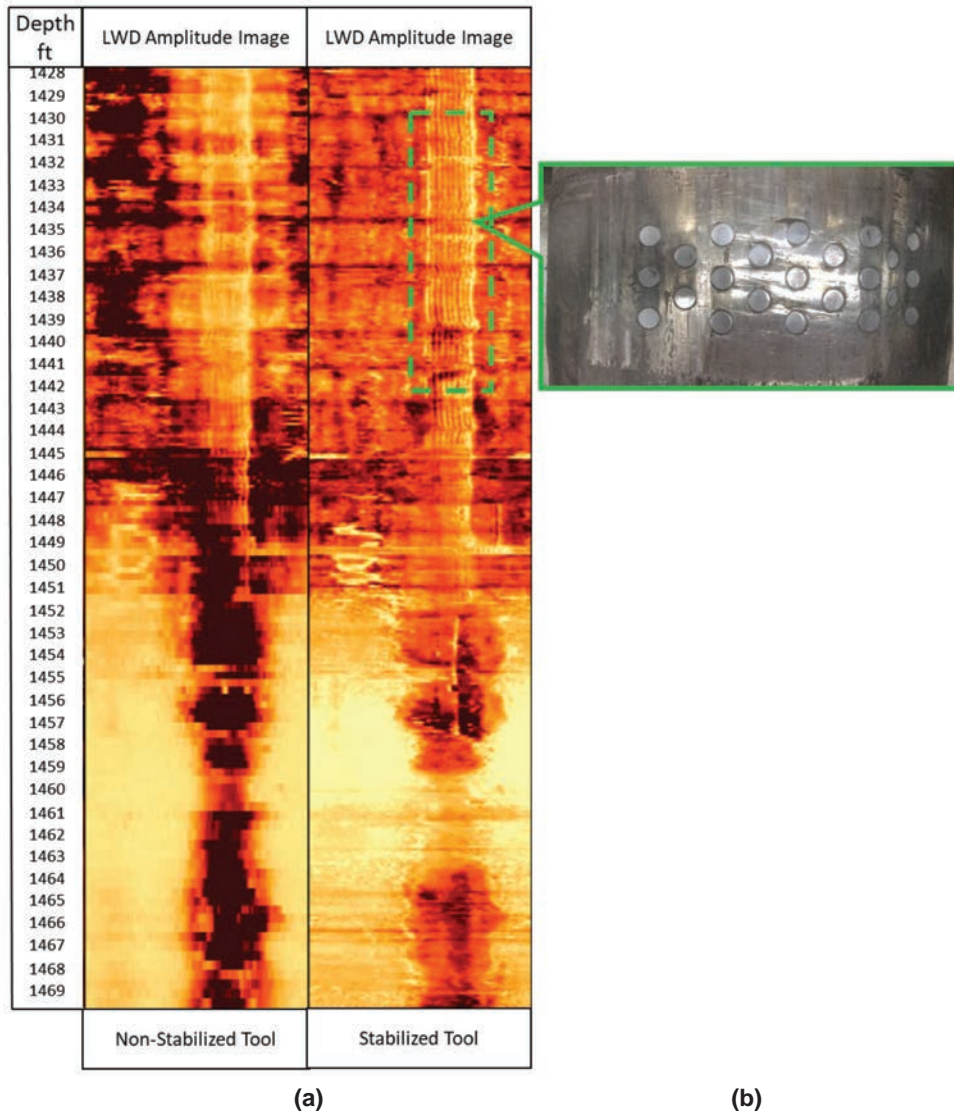


Fig. 23—(a) A comparison of the amplitude images from nonstabilized tool (left) that shows “blurring” and the stabilized tool (right) that shows higher resolution. The vertical striations on the images, highlighted within the dashed-green box, are attributed to gouges made by the kickpad of the mud motor (b).

The fractures observed within the Austin Chalk formation on Well 1 and 2 were again identified on both the high-resolution, 540-sector radius and reflection amplitude images, shown in Fig. 24. The log section also identifies a zone of borehole washout from 1,420 to 1,432 ft, as illustrated by the average borehole size plot (Tracks 4 and 5) and the 3D borehole profiles (Tracks 6 and 7). The reflection amplitude image also shows the same striations believed to be caused by a section of the mud motor that were observed

over the same section in Well 2.

A high-angle section (approximately 80° inclination) of the log within the Rodessa Limestone formation is shown in Fig. 25. Thin laminations, with dip and strike corresponding to the bedding, are clearly visible on the reflection amplitude image, despite the presence of eccentricity and associated large standoff, represented by the dark shading on the radius image.

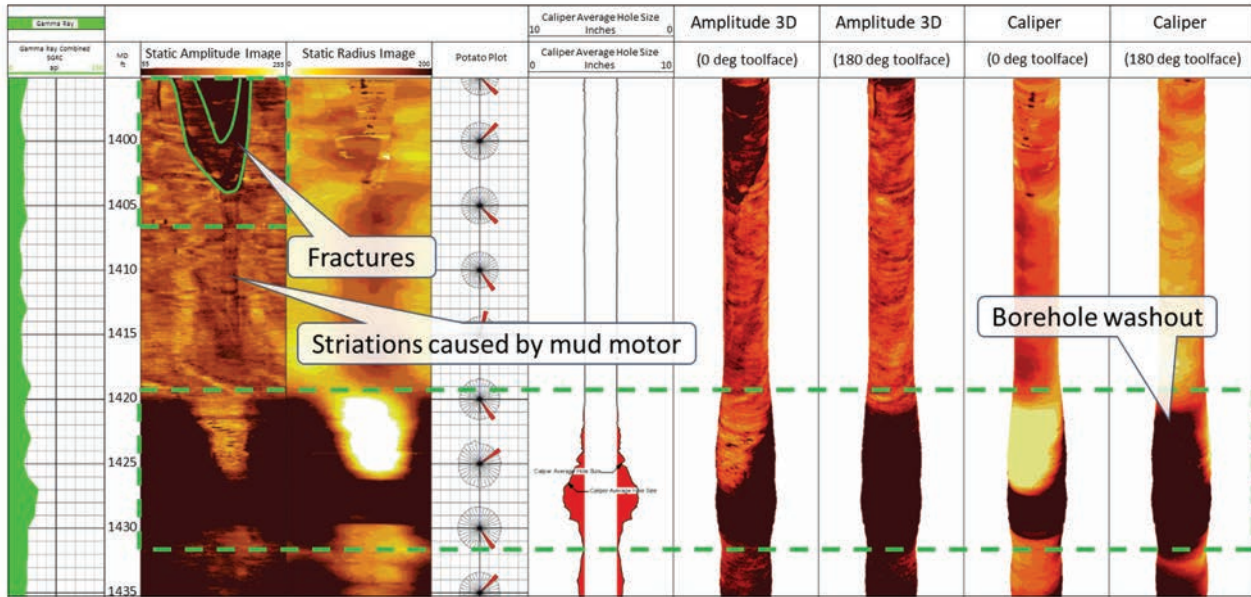


Fig. 24—Log section: Track 1, gamma ray; Track 2, reflection amplitude and radius images; Track 3, potato plots; Track 4, average caliper. Tracks 5 to 8, 3D borehole profile plots across a fracture and borehole washout zone within the Austin Chalk formation.

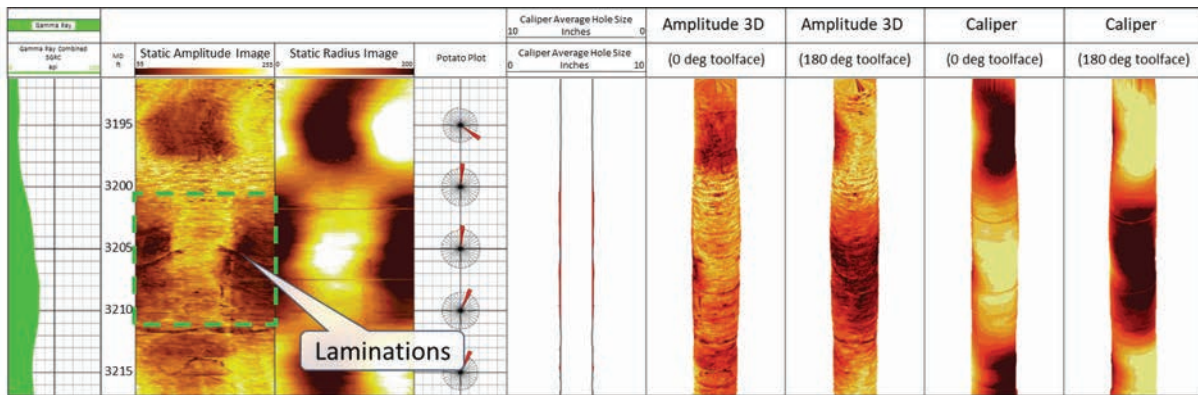


Fig. 25—Log section showing: Track 1, gamma ray; Track 2, reflection amplitude and radius images; Track 3, potato plots; Track 4, average caliper; Tracks 5 to 8, 3D borehole profile plots within an 80° inclination section of the Rodessa Limestone formation.

Bedding features are also visible on the reflection amplitude image taken from a section where the borehole inclination was 87° (Fig. 26). The dark features on both the reflection amplitude and radius images between 3,754 and 3,757 ft are caused by the kickpad on the mud motor at the start of a slide section to drop angle.

The wellbore enabled assessment of both borehole caliper and images in vertical, build, and near-horizontal borehole sections using OBM. The borehole caliper, radius images, and 3D borehole profile plots created from the traveltime measurements identified zones of borehole enlargement, and the high-resolution reflection amplitude images identified fractures and bedding features within multiple formations.

CONCLUSIONS

This paper presents a 4.75-in. LWD ultrasonic imaging tool with four transducers arranged at uniform azimuthal spacings. We demonstrate how the tool’s hardware design and advanced algorithms can compensate for the systematic errors introduced into the caliper and reflection amplitude images by tool center motion. We describe the laboratory testing performed on the transducers using both 2D and 3D apparatus, and measure the potential detection and resolution capabilities of the tool.

Three field tests demonstrate the impact of poor stabilization on both caliper and reflection amplitude

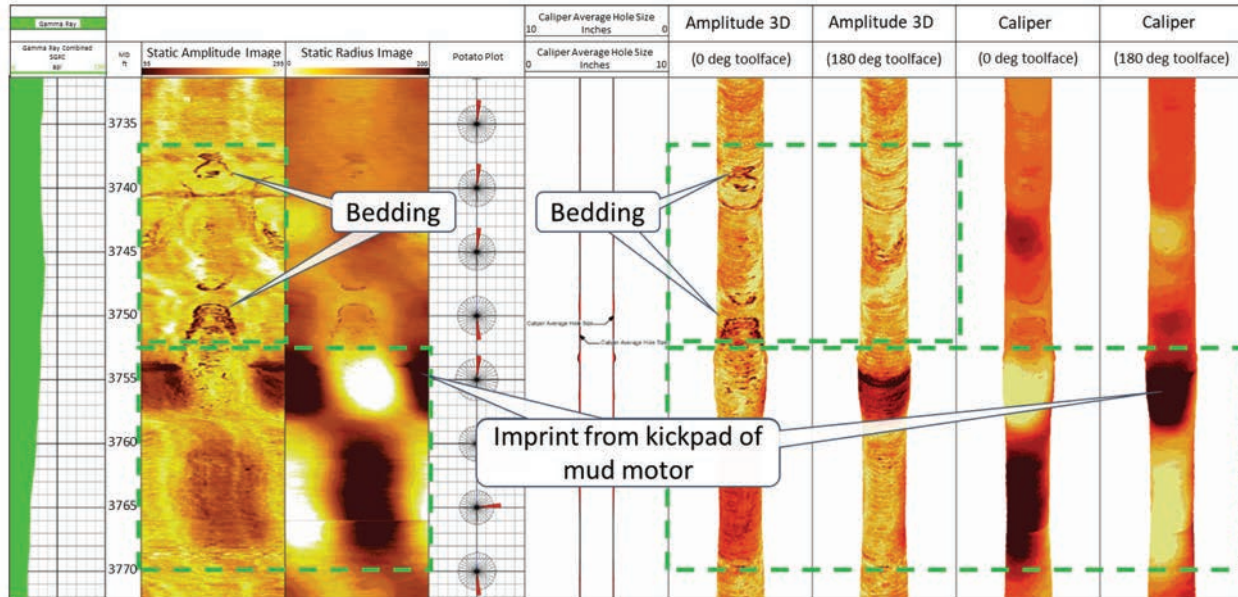


Fig. 26—Log section showing: Track 1, gamma ray; Track 2, reflection amplitude and radius images; Track 3, potato plots; Track 4, average caliper; Tracks 5 to 8, 3D borehole profile plots within a near-horizontal section of the Rodessa Limestone. The section highlighted inside the dashed green boxes represents a slide section to drop inclination where tool marks related to the kickpad of the mud motor are observed at 3,754 ft on the top of the borehole on the amplitude image. The start of the slide sections corresponds to a slight increase in borehole diameter.

images that leads to a recommendation that this tool should be centralized within the borehole using stabilizers with outside diameters that are 0.125-in. smaller than the nominal borehole size, i.e., 0.125-in. undergauge. Comparison of images acquired at different logging and drillstring rotation speeds shows that the resolution of the radius and reflection amplitude images were comparable over a wide range of conditions, although some improvements were seen at low values of the ratio of ROP to RPM, consistent with theory.

The three field tests also demonstrate that the tool is able to produce high-resolution images in both vertical and horizontal borehole sections. From these images we are able to identify fractures, bedding features, and drilling-induced features in multiple formations. The excellent correlation of these results with those from analogous wireline ultrasonic imaging and 6-arm caliper technologies highlights the potential for the 4.75-in. LWD ultrasonic imaging tool to be the primary logging solution in wellbores where the use of wireline may be either risky or costly.

ACKNOWLEDGEMENTS

The authors would like to thank Halliburton for supporting the technologies and publications, and Mohamed Hany for his help in processing the data and preparing the log examples.

REFERENCES

Ballay, G., Hussein, A-A., Amos, S., and Dennis, B., 2001, In the Driver’s Seat With LWD Azimuthal Density Images, Paper SPE-77282 presented at the SPE/IADC Middle East Drilling Technology Conference, Bahrain, 22–24 October. DOI: 10.2118/72282-MS.

Bittar, M., Klein, J., Beste, R., Hu, G., Wu, M., Pitcher, J., Golla, C., Althoff, G., Sitka, M., Minosyan, V. and Paulk, M., 2009, A New Azimuthal Deep-Reading Tool for Geosteering and Advanced Formation Evaluation, Paper SPE-109971, *SPE Reservoir Evaluation & Engineering*, **12**(2), 270–279. DOI: 10.2118/109971-PA.

Davies, D.H., Faivre, O., Gounot, M-T., Seeman, B., Trouiller, J-C., Benimell, D., Ferreira, A., Pittman, D.J., Randrianavony, M., Smits, J.W., Anderson, B.I., and Lovell, J., 1994, Azimuthal Resistivity Imaging: A New-Generation Laterolog, Paper SPE-24676, *SPE Formation Evaluation*, **9**(3), 165–174. DOI: 10.2118/24676-PA.

Ekstrom, M.P., Dahan, C.A., Chen, M.Y., Lloyd, P.M., and Rossi, D.J., 1987, Formation Imaging With Microelectrical Scanning Arrays, *The Log Analyst*, **28**(3), 294–306.

Hayman, A.J., Parent, P., Cheung, P., Verges, P., 1998, Improved Borehole Imaging by Ultrasonics, Paper SPE-28849, *SPE Production & Operation*, **13**(1), 5–14. DOI: 10.2118/28440-PA.

Joyce, B., Patterson, D., Leggett, J., and Dubinsky, V., 2001, Introduction of a New Omni-Directional Acoustic System

for Improved Real-Time LWD Sonic Logging—Tool Design and Field Test Results, Paper SS, *Transactions, SPWLA 42nd Annual Logging Symposium*, Houston, Texas, USA, 17–20 June.

- Labat, C., Brady, S., Everett, M., Ellis, D., Doghmi, M., Tomlinson, J., and Shehab, G., 2002, 3D Azimuthal LWD Caliper, Paper SPE-77526 presented at the SPE Annual Technical Conference and Exhibition, San Antonio, Texas, USA, 29 September–2 October. DOI: 10.2118/77526-MS.
- Li, P., Lee, J., Taher, A., Coates, R., and Marlow, R., 2019, New 4¾-in. High-Resolution Ultrasonic Borehole Imaging for Unconventional Reservoir Evaluation. Paper URTEC-2019-322, Unconventional Resources Technology Conference, 22–24 July. DOI: 10.15530/urtec-2019-322.
- Li, Q., Omeragic, D., Chou, L., Yang, L., Lau, T., Liu, C., Dworak, R., Dreullault, V., and Ye, H., 2005, New Directional Electromagnetic Tool for Proactive Geosteering and Accurate Formation Evaluation While Drilling, Paper UU, *Transactions, SPWLA 46th Annual Logging Symposium*, New Orleans, Louisiana, USA, 26–29 June.
- Morys, M., Chemali, R., Goodman, G., Smollinger, G., Schaecher, B., and Maki, V., 2011, Field Testing of an Advanced LWD Imager for Oil-Based Mud Applications, *Petrophysics*, 52(2), 84–95.

ABOUT THE AUTHORS



Peng Li is Senior R&D Advisor at Halliburton Sperry Drilling. He holds a BSc in the School of Automation Science and MSc in Electrical Engineering from Beihang University, and a PhD degree in Control from the University of Houston. He has worked on a variety of downhole logging technologies including ultrasound

borehole imaging and casing evaluation, electromagnetic-based casing-corrosion detection, and nuclear magnetic resonance logging. His research interests include control and signal processing, embedded systems and instrumentation, motor control and power electronics, and wireless sensor network and high-speed digital communications.



Jonathan Lee is Product Manager for Acoustic and Magnetic Resonance at Halliburton Sperry Drilling. He began his career as a mudlogger in the North Sea with Exlog, before moving to various MWD/LWD field positions. He has since held various product management and business development positions in Houston with Baker Hughes, GE, and TGT Oil & Gas Services. He holds a BSc in geology from the University of Wales, Cardiff, and is a member of SPE and SPWLA.



Richard Coates is currently Chief R&D Advisor at Halliburton Sperry Drilling. Prior to joining Halliburton, he spent most of his career with Schlumberger working on sonic and seismic topics in a variety of technical and management roles, culminating as a Scientific Advisor. Prior to joining Schlumberger, he was a Post-Doctoral Fellow at the Earth Resources Lab., MIT. He holds a MA in Natural Sciences (Physics) and a PhD in Geophysics from the University of Cambridge, and is a member of the EAGE, SEG and SPWLA. He is an Associate Editor of the SPWLA journal *Petrophysics* and Associate Editor of the SEG journal *Geophysics*.



Jing Jin is a Scientific Advisor at Halliburton Sperry Drilling, working on the development of ultrasonic transducers for LWD technologies. Prior to joining Halliburton, he was Head of Department at Microfine, focused on the R&D of piezoelectric transducers. He then joined Halliburton as principle mechanical engineer, working on the development of piezoelectric transducers for both wireline and LWD sensors. He has 20 published papers and five patents awarded. He holds a BE in Civil Engineering and a MSc in Structural Engineering from Shanghai Jiaotong University, and a PhD in Civil Engineering from the National University of Singapore.



Siong (Hans) Ming Wong is a Senior Technical Advisor in the Global Technical Services group at Halliburton Sperry Drilling, providing technical assistance across multiple MWD/LWD technologies. He began his career with Halliburton in 2003 as a MWD/LWD field engineer, before moving to Service Quality and QA Engineer roles. He holds a BEng Hons Degree in Petroleum Engineering from the University of Malaysia and serves as 2019–2020 Secretary of the Houston SPWLA Chapter.